Interference, Dephasing, and Coherent Control in Time-Resolved Frequency Domain Two-Dimensional Vibrational Spectra

Kent A. Meyer and John C. Wright*

Department of Chemistry, 1101 University Avenue, University of Wisconsin, Madison, Wisconsin 53706

Received: April 28, 2003; In Final Form: July 10, 2003

The amplitude level quantum interference between different coherence pathways in doubly vibrationally enhanced four wave mixing (DOVE-FWM) can be used to control the relative intensities of different features in the two-dimensional vibrational spectrum of CS_2 in CH_2BrCl. The relative intensity reflects the final state populations that are controlled by the FWM processes. Modeling of the time dependent frequency-domain 2D spectra shows how the interference between pathways and their relative dephasing rates are responsible for the ability to control the relative intensity changes.

Introduction

Continuing advances in the generation of coherent infrared light have stimulated great interest in coherent multidimensional vibrational spectroscopy (CMDVS) because of its potential for probing molecular interactions.[1] CMDVS techniques use a series of optical pulses that create multi-quantum vibrational coherences that are analogous to the nuclear spin coherences in multidimensional NMR experiments.[2] The multiple quantum coherences are responsible for cross-peaks between vibrational modes that are coupled, just as cross-peaks appear in NMR spectra from nuclear couplings.[3,4] Multidimensional techniques are useful because they can resolve the spectral information in congested spectra, and they can probe specific couplings between modes in order to provide structural information.

Although all nonlinear optical methods are capable of multidimensional spectroscopy, most attention has focused on nonlinear four-wave mixing (FWM) techniques. FWM techniques use three excitation pulses to create a series of coherences in a sample that subsequently radiate the signal that is detected. Doubly vibrationally enhanced FWM (DOVE-FWM) is one example that focuses two infrared pulses with frequencies at ω_1 and ω_2 and one visible pulse at ω_3 into a sample, creating an output pulse at $\omega_4 = \omega_1 - \omega_2 + \omega_3$. The infrared pulses are tuned near vibrational transitions in the sample, while the visible pulse is fixed in frequency and is not resonant with vibrational transitions. The output signal is strongly enhanced when the two infrared pulses are tuned to coupled vibrations but is not enhanced when tuned to uncoupled transitions.[5] There are three important pathways by which the successive excitation steps create the final coherence that generates the output signal. These pathways interfere at the amplitude level and are the basis for controlling the relative intensities of the spectral features. The relative intensities are a measure of the relative final state populations that result after the nonparametric four wave mixing.

There is a close relationship between the pathways involved in coherent multidimensional spectroscopy and coherent control applications. The amplitude level interferences between different coherence pathways form the basis for coherent quantum control. In time domain coherent control, the temporal profile of an ultrafast pulse is designed to modulate the instantaneous phase, frequency, and amplitude of the coherent excitation so amplitude level interference between parallel coherence pathways can control the relative importance of different product states.[6−11] For simple systems, the optimum temporal profile can be understood from an analysis of the states that must participate in the pathways but for complex systems, adaptive genetic algorithms search for optimum temporal profiles.

Recent DOVE-FWM measurements of carbon disulfide excited the IR-active anti-symmetric stretch (ν_3) and a combination band involving the symmetric and anti-symmetric stretch modes ($\nu_1 + \nu_3$).[12] The experiment used an ultrafast (~1 ps) laser system to generate the DOVE-FWM signals as well as nonresonant nonlinear processes that provided a background. Because the nonresonant processes dephase very quickly, it was possible to include delays between the excitation pulses to temporally discriminate between the DOVE and nonresonant signals. The large DOVE signal and the excellent temporal discrimination allowed one to obtain low detection limits for CS_2.

In this paper, we report a series of two-dimensional spectra for CS_2 as a function of the delay times between excitation pulses. The spectra show strong variations in the relative importance of the DOVE, singly vibrationally resonant coherent anti-Stokes Raman scattering (CARS) peaks, and the nonresonant background. These changes occur because of quantum level interference between different coherence pathways as well as differences in their relaxation rates. In particular, the two DOVE-IR pathways destructively interfere with the DOVE-Raman pathway. The DOVE-IR and DOVE-Raman pathways differ in the frequency of an intermediate coherence because of the anharmonic shift induced by coupling. Therefore, the interference is observed as a beat at the frequency of the anharmonic shift, which modulates the dominant feature in the two-dimensional spectrum. This observation demonstrates that quantum control of two-dimensional vibrational spectra is possible. Here, one can suppress or enhance particular spectral features by controlling the quantum interference effects. Such quantum interferences between different coherence pathways are closely related to the processes that quantum control methods

---

* Corresponding Author. E-mail: wright@chem.wisc.edu.

10.1021/jp035146+ CCC: $25.00

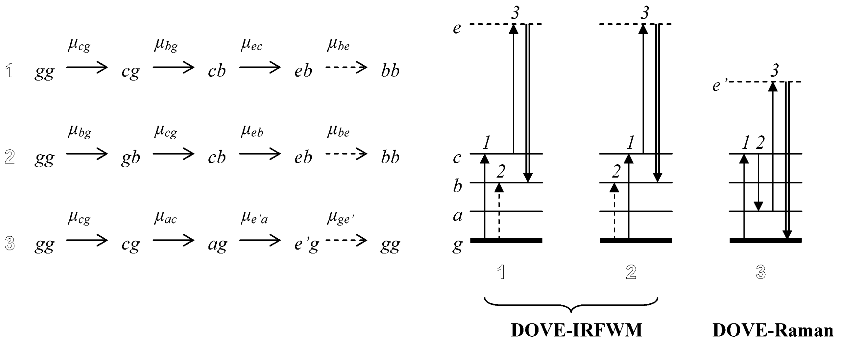

Figure 1. A selection of FWM Liouville pathways that involve three excitation fields and an output field such that $\omega_4 = \omega_1 - \omega_2 + \omega_3$. Along a given pathway, each electric field interaction changes either the left (ket) or right (bra) index of the density matrix element jk. The double line in the last step represents the output signal. Solid horizontal lines in the energy level diagrams at right indicate vibrational levels, while dashed lines represent virtual levels. The electric fields responsible for each change are numbered accordingly. The arrows are solid if the ket changes and dotted if the bra changes. CARS is similar to the DOVE-Raman pathway, but has a virtual state located at c instead.

use to steer chemical reactions.[6−11] The spectra can be simulated with a perturbative frequency domain model that allows us to estimate the dephasing rates and the multidimensional third-order susceptibilities $\chi^{(3)}$ of the interfering coherence pathways.[13] The $\chi^{(3)}$ values are compared to expected values based on IR and Raman data.

Experimental Section

The experimental apparatus used for the picosecond DOVE experiment has been described previously.[12] The excitation beams are two independently tunable infrared beams (ω_1, ω_2) and one fixed-frequency near-visible beam ($\omega_3 = 12650$ cm^{-1}) with approximate temporal pulse-widths of 1 ps and bandwidths of 25 cm^{-1} (fwhm). They were generated by a Ti/sapphire regenerative amplifier system with a repetition rate of 1.0 kHz. The three beams were focused into a 150-μm thick sample consisting of CS_2 diluted in bromochloromethane along with an optically oriented 150 μm sapphire front window and a 150-μm borosilicate glass back window. The nominal CS_2 concentration of the samples was 0.20 M. The beams ω_1 and ω_3 were sent into the sample nearly collinearly, while an angle of 7.7° was applied to ω_2 to achieve an approximate phase-matching condition for the sample. For dilute CS_2, ω_1 was tuned near the ($\nu_1 + \nu_3$) combination band at 2169 cm^{-1}, and ω_2 was tuned to the ν_3 anti-symmetric stretch at 1520 cm^{-1}. Delay stages were used with two of the pulses in order to create adjustable delays (τ_1, τ_2) between the ω_1 and ω_2 and ω_2 and ω_3 beams, respectively. The two-dimensional spectra for different time delays were performed on separate samples. The measured CS_2 concentrations were 0.26, 0.15, 0.10, and 0.30M for the (τ_1,τ_2) values (0,0), (0,2), (0,4), and (1,3) ps delays, respectively. The beam polarizations were all parallel, so the signal results solely from $\chi^{(3)}_{1111}$. The apparatus was purged with N_2 to remove interferences from atmospheric H_2O and CO_2.

Coherent FWM signal was detected at $\omega_4 = \omega_1 - \omega_2 + \omega_3$ using a scanning monochromator with 25 cm^{-1} band-pass filter and a photomultiplier. Two-dimensional spectra were generated by scanning ω_1 in units of 2 cm^{-1} with ω_2 steps of 5 or 10 cm^{-1}. Each data point is an average of 1000 shots per point. Scans were normalized to the intensity of the scanned beam ω_1 and referenced to CH_2BrCl's observed coherent anti-Stokes Raman scattering (CARS) feature at 601 cm^{-1}.

Theoretical Background

Our model for simulating the coherent 2D-DOVE spectra uses conventional perturbation theory to treat the oscillating electric fields' interactions with a chemical system.[13] The fields create a series of coherences between states j and k that can be described by off-diagonal density matrix elements ρ_{jk} and populations that are described by diagonal density matrix elements ρ_{jj}. Coherences and populations rapidly evolve after the interaction, but may be intercepted by a second electric field that drives a second coherence or population. Multiple interactions can therefore define time-ordered pathways of ρ_{jk}'s such as those seen in Figure 1. Optical processes usually start with the system in an initial ground-state population and end with a final radiating coherence. Maxwell's equations relate the coherence's oscillating polarization to the radiated electric field. Because several pathways may contribute to the final ρ_{jk}, all pathways must be considered in order to account for interferences.

For DOVE-FWM, only pathways involving vibrational states near the frequency of ω_1 and ω_2 or involving off-resonant electronic states are considered. Other pathways make negligible contributions. The most important pathways for creating $\omega_4 = \omega_1 - \omega_2 + \omega_3$ output are illustrated in Figure 1. Although the states labeled g, a, b, c, and e can represent any state, this paper will assume that g is the ground state, a and b are the ν_3 and ν_1 modes, respectively, c is the $\nu_1 + \nu_3$ combination band, and e is a nonresonant electronic state. DOVE-IR-FWM consists of two pathways, each of which is doubly vibrationally enhanced when ω_1 is tuned to a vibrational mode and ω_2 is tuned to a second, coupled vibrational mode. DOVE-Raman-FWM is doubly enhanced when ω_1 and $\omega_1 - \omega_2$ are tuned to coupled vibrational modes. In addition to the DOVE processes, there are other processes that can make a contribution to the overall FWM signal. Coherent anti-Stokes Raman scattering (CARS) is a singly enhanced process occurring when $\omega_1 - \omega_2$ is tuned near a vibration. Finally, the background FWM is not vibrationally enhanced and occurs at all frequencies in the FWM spectrum.

The excitation electric fields are defined by

$$\vec{E}_n(\vec{k}_n,t) = \frac{1}{2}E_n^0\tilde{E}_n(t)(e^{i(\vec{k}_n z - \omega_n t)} + e^{-i(\vec{k}_n z - \omega_n t)})$$

where E_n^0 are the peak amplitudes and $\tilde{E}_n(t)$ are the temporal envelopes of the fields, while the output nonlinear polarization is defined by[14]

$$\vec{P}_4(\vec{k}_4,t) = E_1^0\, E_2^0\, E_3^0(P^0(t)e^{i(\vec{k}_4 z - w_4 t)} + P^{0*}(t)e^{-i(\vec{k}_4 z - w_4 t)})$$

TABLE 1: Components of the Major Coefficients *A* Used in the Fitting Procedure

$A_{\mathrm{DOVE-IR}}$	$\alpha_{\mathrm{cb}}\mu_{\mathrm{gb}}\mu_{\mathrm{gc}}$
$A_{\mathrm{DOVE-Raman}}$	$\alpha_{\mathrm{ag}}\mu_{\mathrm{ca.}}\mu_{\mathrm{gc}}$
A_{CARS}	$\alpha_{\mathrm{ag}}\alpha_{\mathrm{ga}}$

In the limit of homogeneous broadening, the final forms of $P^0(t)$ for each of the important FWM processes in this DOVE experiment are

$$P^0_{\mathrm{DOVE-IR_1}}(t) = -A_{\mathrm{DOVE-IR1}}\left(\frac{1}{2}\right)^3 NF(\omega_1)F(\omega_2)F(\omega_3)\tilde{E}_3(t) \times \left(\frac{i}{\hbar}\right)^2 \int_0^\infty \mathrm{d}t_2\theta(t_2)\tilde{E}_2(t-t_2+\tau_2)e^{-\Gamma_{\mathrm{cb}}t_2}e^{i(\omega_1-\omega_2-\omega_{\mathrm{cb}})t_2}\int_0^\infty \mathrm{d}t_1 \times \theta(t_1)\tilde{E}_1(t-t_2-t_1+\tau_2+\tau_1)e^{-\Gamma_{\mathrm{cg}}t_1}e^{i(\omega_1-\omega_{\mathrm{cg}})t_1} \quad (1a)$$

$$P^0_{\mathrm{DOVE-IR_2}}(t) = -A_{\mathrm{DOVE-IR2}}\left(\frac{1}{2}\right)^3 NF(\omega_1)F(\omega_2)F(\omega_3)\tilde{E}_3(t) \times \left(\frac{i}{\hbar}\right)^2 \int_0^\infty \mathrm{d}t_2\theta(t_2)\tilde{E}_1(t-t_2+\tau_2+\tau_1) \times e^{-\Gamma_{\mathrm{cb}}t_2}e^{i(\omega_1-\omega_2-\omega_{\mathrm{cb}})t_2}\int_0^\infty \mathrm{d}t_1\theta(t_1)\tilde{E}_2(t-t_2-t_1+\tau_2) \times e^{-\Gamma_{\mathrm{bg}}t_1}e^{i(-\omega_2-\omega_{\mathrm{gb}})t_1} \quad (1b)$$

$$P^0_{\mathrm{DOVE-Raman}}(t) = A_{\mathrm{DOVE-Raman}}\left(\frac{1}{2}\right)^3 NF(\omega_1)F(\omega_2)F(\omega_3)\tilde{E}_3(t) \times \left(\frac{i}{\hbar}\right)^2 \int_0^\infty \mathrm{d}t_2\theta(t_2)\tilde{E}_2(t-t_2+\tau_2)e^{-\Gamma_{\mathrm{ag}}t_2}e^{i(\omega_1-\omega_2-\omega_{\mathrm{ag}})t_2}\int_0^\infty \mathrm{d}t_1 \times \theta(t_1)\tilde{E}_1(t-t_2-t_1+\tau_2+\tau_1)e^{-\Gamma_{\mathrm{cg}}t_1}e^{i(\omega_1-\omega_{\mathrm{cg}})t_1} \quad (1c)$$

$$P^0_{\mathrm{CARS}}(t) = A_{\mathrm{CARS}}\left(\frac{1}{2}\right)^3 NF(\omega_1)F(\omega_2)F(\omega_3)\tilde{E}_3(t) \times \left(\frac{i}{\hbar}\right)\int_0^\infty \mathrm{d}t_1\theta(t_2)\tilde{E}_2(t-t_1+\tau_2)\tilde{E}_1(t-t_1+\tau_2+\tau_1) \times e^{-\Gamma_{\mathrm{ag}}t_1}e^{i(\omega_1-\omega_2-\omega_{\mathrm{ag}})t_1} \quad (1d)$$

$$P^0_{\mathrm{BG}}(t) = A_{\mathrm{BG}}\left(\frac{1}{2}\right)^3 NF(\omega_1)F(\omega_2)F(\omega_3)\tilde{E}_3(t)\tilde{E}_2(t+\tau_2) \times \tilde{E}_1(t+\tau_2+\tau_1) \quad (1e)$$

where N is the number density, $F(\omega) = (n^2(\omega) + 2)/3$ is the local field correction,[16] Γ_{ij} and ω_{ij} are the dephasing rate and the transition frequency for the i−j transition, t represents the time when the third field generates the output Raman transition, τ_1 and τ_2 represent the time delays between pulses 1 and 2 and pulses 2 and 3, respectively, and t_1 and t_2 are the difference in the interaction times between the fields. It is important to recognize that the subscript on the field labels the frequency of the field, not the time ordering of the pulses as is common in photon echo and transient grating FWM. The subscript on the time, however, labels the time intervals between successive interactions.

The simplifications in eq 1 include using the rotating wave[13] and the Placzek approximations.[15] The rotating wave approximation[13] eliminates terms that do not have double vibrational resonances. The Placzek approximation reduces the number of convolutions by assuming that coherences involving virtual levels respond instantaneously to the applied field. The coefficients A can then be defined (see Table 1) in terms of the vibrational transition dipoles and electronic polarizabilities for each pathway. We also confine the study to χ_{1111}. For carbon disulfide, the modes probed in this experiment (ν_1, ν_3, and $\nu_1 + \nu_3$) are identically polarized so this tensor element dominates. The initial ground-state population is taken as unity. $\theta(t)$ is the Heaviside function. The electric fields generated by our system are approximately Gaussian

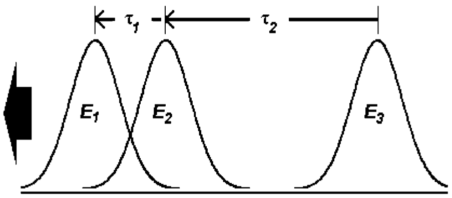

Figure 2. The pulse arrangement for the picosecond FWM experiment have delays τ defined by the above diagram. The dark arrow represents the direction of propagation of the beams entering a sample.

$$\tilde{E}_n(t') = \exp\left(-\frac{t'^2}{2\sigma_n^{\,2}}\right)$$

with relative times τ_1 and τ_2 between the pulses as seen in Figure 2.

Each launched electric field is proportional to the associated polarization, and the overall intensity can be readily solved using Maxwell's equations. After integrating along the path length z, the signal intensity is

$$I(\omega_4) \propto \frac{\omega_4^{\,2}F^2(\omega_4)}{n(\omega_4)}|M_{\mathrm{s}}l_{\mathrm{s}}\int_{-\infty}^{\infty}\sum P(t)\mathrm{d}t|^2$$

with l_{s} being the thickness of the sample. This result assumes that $P^0(t)$ varies slowly with respect to an optical cycle. The factor M_{s} accounts for phase-matching and absorption effects, as well as interferences from the sample cell windows[17]

$$M_{\mathrm{s}} = \frac{\exp(i\Delta k_{\mathrm{fw}}l_{\mathrm{fw}} - \Delta\alpha_{\mathrm{fw}}l_{\mathrm{fw}})(\exp(i\Delta k_{\mathrm{s}}l_{\mathrm{s}} - \Delta\alpha_{\mathrm{s}}l_{\mathrm{s}}) - 1)}{i\Delta k_{\mathrm{s}}l_{\mathrm{s}} - \Delta\alpha_{\mathrm{s}}l_{\mathrm{s}}}$$

Here, $\Delta\alpha$ and Δk are the sums of attenuation factors and wavevectors at each excitation frequency for the front window and the sample.[18] The back window is not a factor of M_{s}, but additional FWM signal coming from the windows can interfere with the signal. They add to the total intensity using similar equations.[18,19]

Multidimensional frequency domain spectra require Fourier transforms of the time variable in equations (1a−e). In the limit of short-time or frequency-narrowed excitations, the convolutions become simple integrals that result in a frequency dependent susceptibility.[13]

There are two important cases where the coherences in equations (1a−e) interfere with each other. In the first case, the oscillatory parts of the first integral in the two DOVE-IR pathways both depend on ($\omega_1-\omega_2-\omega_{\mathrm{cb}}$), while the second integral depends on ($\omega_1-\omega_{\mathrm{cg}}$) in the first DOVE-IR pathway and ($-\omega_2-\omega_{\mathrm{gb}}$) for the second DOVE-IR pathway. The peaks for each pathway occur at the same frequencies in two-dimensional spectra and since they have the same sign, they constructively interfere with each other. In the second case, the oscillatory parts of the first integral in the DOVE-Raman pathway depends on ($\omega_1-\omega_{\mathrm{cg}}$), but the second integral depends on ($\omega_1-\omega_2-\omega_{\mathrm{ag}}$). This resonance occurs at a different frequency than the ($\omega_1-\omega_2-\omega_{\mathrm{cb}}$) resonance in the two DOVE-IR pathways. The pathways destructively interfere because they have the opposite signs, but their peak values do not occur at the

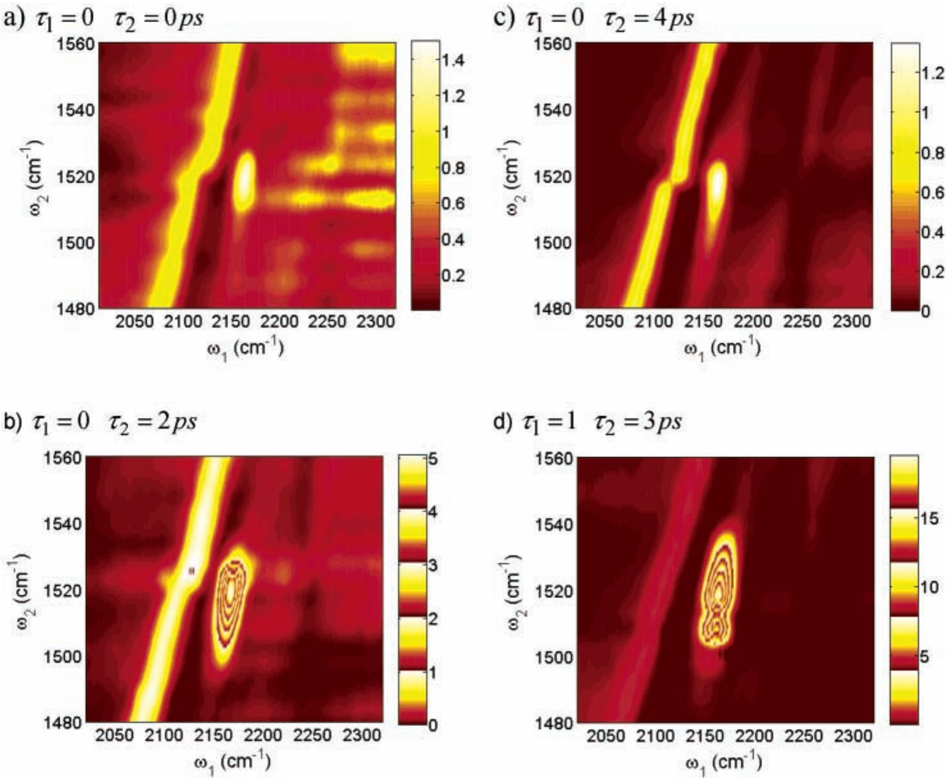

Figure 3. Experimental 2D spectra for the four time delays indicated in the figure.

same frequencies. The DOVE-IR pathway peaks occurs when (ω_1, $\omega_1-\omega_2$) = (ω_{cg}, ω_{cb}) and (ω_2, $\omega_1-\omega_2$) = (ω_{bg}, ω_{cb}) while the DOVE-Raman pathway peak occurs when (ω_1, $\omega_1-\omega_2$) = (ω_{cg}, ω_{ag}). The two DOVE-IR pathways' peaks overlap but the DOVE-Raman peak is offset by the anharmonicity, ($\omega_{cb}- \omega_{ag}$). Thus, the interference will appear as a beat pattern that oscillates with a period of $2\pi/(\omega_{cb}-\omega_{ag})$.

Results and Discussion

Experimental and Simulated Two-Dimensional Vibrational Spectra. Vibrational coherences typically involve dephasing times $1/\Gamma_{jk}$ of ~1 ps, whereas the virtual state coherences of the background dephase almost instantaneously. When the pulse width is less than $1/\Gamma_{jk}$, the DOVE signal-to-background ratio can be increased by delaying the pulse directly after the creation of a vibrational coherence. Such a technique can be used to remove the signal/nonresonant background ratio problem that is prevalent in nonlinear spectroscopy using narrow bandwidth lasers.[20,21] Equations (1a–e) also show that CARS signal decreases as a function of τ_1, because it requires the convolved temporal overlap of pulses 1 and 2, whereas the DOVE signal decreases by the exponential related to the first coherence in the DOVE-IR and DOVE-Raman pathways. Delays can therefore suppress the CARS features of any sample component.

There are many systems with dephasing times longer than 1 ps.[22] For example, picosecond CARS spectroscopy determined the ρ_{ag} vibrational coherence time for the ν_1 mode of dilute CS_2 as ~30 ps.[23] This ρ_{ag} coherence is closely related to ρ_{cb}, which involves the fundamental ν_3 mode of CS_2 at 1520 cm^{-1} and the combination band $\nu_1 + \nu_3$ at 2167 cm^{-1}. In both cases, the coherence involves the oscillation of the ν_1 mode, but they differ in whether the ν_3 mode is excited. Anharmonicity shifts the frequency of the combination band from that expected for the sum of the two fundamentals. The anharmonicity is evidence of the coupling that makes the combination band detectable. DOVE-FWM at these frequencies would then generate a coherence ρ_{cb} with a dephasing rate of similar time scales to the ρ_{ag} vibrational coherences. With the lasers used in this experiment, it should be possible to use temporal discrimination to enhance the signal-to-background ratio.

FWM spectra taken of the different CS_2/CH_2BrCl mixtures and their fits are shown in Figures 3 and 4 with τ_1 and τ_2 specified for each spectrum. Zero delay was determined using cross-correlation with nonresonant background. Parameters that were fixed in the fits are shown in Table 2. Several of these parameters come from fits of the IR and Raman data at this concentration and are designated accordingly. The line-widths Γ_{cg}, Γ_{bg}, and Γ_{ag} are equal to the line-widths of the corresponding bands in the IR and Raman spectra. In the IR and Raman spectra, there are contributions in the 1520 cm^{-1} υ_3 mode from hot-bands involving the 350 cm^{-1} υ_2 mode of CS_2 where (υ_2, υ_3) → (υ_2, $\upsilon_3 + 1$). The corresponding contributions were not evident in the DOVE spectra in Figure 3. The most noted features in the spectra are the diagonal CH_2BrCl CARS feature at ($\omega_1-\omega_2$) = 601 cm^{-1} and the peak at (ω_1, ω_2) = (2165.5, 1517) cm^{-1}. The latter peak corresponds to the expected DOVE-IR feature of CS_2 at these frequencies. The corresponding peak in the Raman and infrared spectrum of the dilute sample is shifted in frequency from neat CS_2 solution, and it is narrower because of the inhomogeneous broadening that occurs in the neat solution. The widths of the CARS and DOVE signals are larger in Figure 3 than the line-widths of the Raman and infrared features of the mixture because the ultrafast infrared excitation pulses have a broad frequency distribution. The intensity of each scan in Figures 3 and 4 were normalized to the $\omega_1-\omega_2$ = 601 cm^{-1} line because it is singly resonant and its intensity depends only on $\omega_1-\omega_2$. The DOVE peak in Figure 3b appears to be resolved into two features, but we believe this behavior results from error in the intensity of the internal standard peak

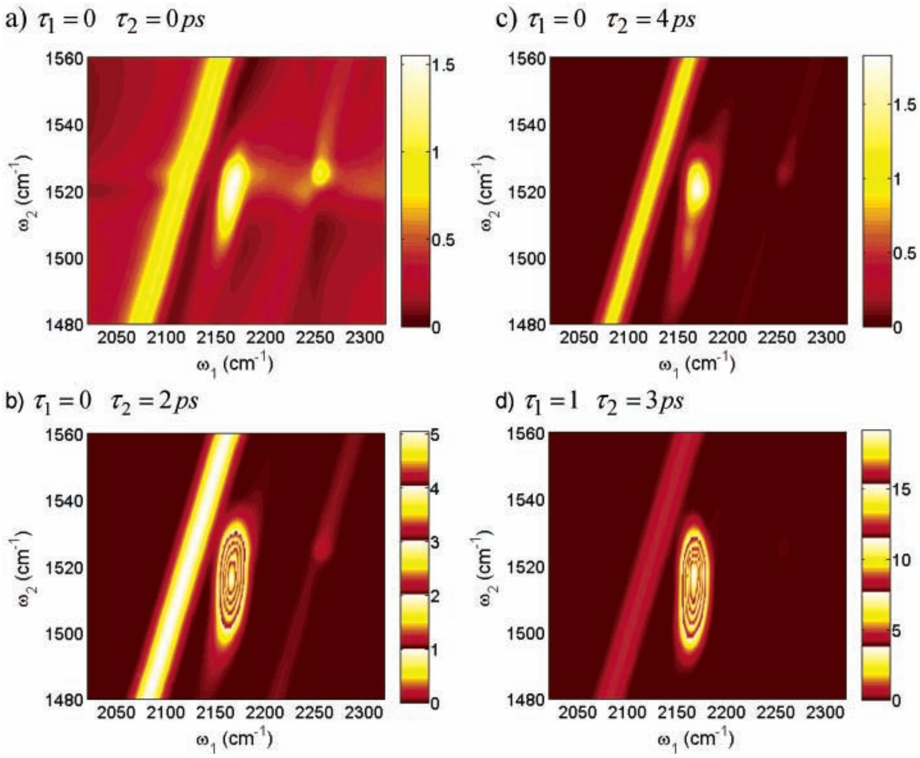

Figure 4. Simulation of the 2D spectra for the four time delays indicated in the figure. The simulation parameters appear in Table 3. The simulation of (τ_1, τ_2) = (1 ps, 3 ps) uses values of (1.2, 2.8 ps), approximately the uncertainty of the absolute delay times.

TABLE 2: Resonance Frequencies and Linewidths (HWHM)[a]

Important FWM transitions							
CS_2	ν_1	ω_{ag}	656	CH_2BrCl	ν_5	$\omega_{ag}{}'$	606
	(sym)	Γ_{ag}	0.18[a]		(C−Br)	$\Gamma_{ag}{}'$	5.3
	ν_3	ω_{bg}	1520				
	(anti-sym)	Γ_{bg}	2.8		ν_4	$\omega_{ag}{}''$	722
	$\nu_1 + \nu_3$	ω_{cg}	2167		(C−Cl)	$\Gamma_{ag}{}''$	10.
		Γ_{cg}	3.5				
Current FWM simulations							
CS_2	ν_1	ω_{ag}	656	CH_2BrCl	ν_5	$\omega_{ag}{}'$	601
		Γ_{ag}	0.18			$\Gamma_{ag}{}'$	1.4
	ν_3	ω_{bg}	1518				
		Γ_{bg}	2.8				
	$\nu_1 + \nu_3$	ω_{cg}	2165.5				
		Γ_{cg}	3.4				

[a] All units are in cm^{-1}. [b] Found from Lorentzian fits in IR and Raman spectra at the concentrations similar to that used in the FWM experiment. [c] From Aechtner et al., ref 23.

that is used to normalize each component spectrum in the two-dimensional spectrum.

Other major features in these spectra are the background signal that appears at all other frequencies and a slight dip in the background at $\omega_1 = 2245$ cm^{-1} due to a weak CH_2BrCl absorption. The background is brighter on one side of the spectrum, at least partly due to phase-matching errors. CH_2BrCl has an additional, weak CARS feature located at $\omega_1 - \omega_2 = 728$ cm^{-1}. The minor absorption of CH_2BrCl and the weak CARS feature intersect on this spectrum, leading to the possibility of a DOVE peak there, but any DOVE peak at that location is insignificant compared to the background.

Interference, Dephasing, and Coherent Control of Relative Intensities in Two-Dimensional Spectra. We can now examine the differences that occur with each spectrum as the time delays are changed. When the pulses are fully overlapped, $\tau_1 = 0$ and $\tau_2 = 0$ (Figure 3a), there is a significant amount of background FWM signal present. The DOVE/background peak intensity ratio is 4:1. The ratio increases to 12:1 as the time delays of the pulses increase to $\tau_1 = 0$ and $\tau_2 = 2$ ps (Figure 3b). When the time between the two infrared pulses increases to $\tau_1 = 0$ and $\tau_2 = 4$ ps (Figure 3c), the ratio decreases to 3.5:1. Finally, when the first time delay is changed to $\tau_1 = 1$ and $\tau_2 = 3$ ps (Figure 3d), the DOVE feature becomes very large (DOVE/background ratio is 50:1) relative to the CARS feature and the background. Additional scans of DOVE and the reference CARS peak show that the DOVE-to-CARS ratio increases dramatically at longer τ_1 times. These data provide firm evidence for the suppression of CARS and background features by temporal discrimination.

It is possible to estimate the double quantum coherence linewidth Γ_{cb} by fitting the line shapes, because the interferences between DOVE pathways depends on these dephasing rates. The expression for Γ_{cb} is given by

$$\Gamma_{cb} = \frac{\Gamma_{cc} + \Gamma_{bb}}{2} + \Gamma^*_{cb}$$

where Γ_{cc} and Γ_{bb} are the population relaxation rates of the combination band and the asymmetric stretch respectively, and Γ^*_{cb} is the pure dephasing rate of the cb coherence.[24] In the absence of population relaxation effects, one expects that $\Gamma^*_{cb} \approx \Gamma^*_{ag} = \Gamma_{ag} \approx \Gamma_{cb}$, assuming state c is a combination band of a and b. Using the values in Table 2, $\Gamma_{cb} = 0.18$ cm^{-1} in this limit. If population relaxation dominates, $\Gamma_{cc} = 2\Gamma_{cg}$, Γ_{bb}=$2\Gamma_{bg}$, and so $\Gamma_{cb} = \Gamma_{cg} + \Gamma_{bg}$. Using the values in Table 2, $\Gamma_{cb} = 6.3$ cm^{-1} in this limit. The simulations were fit with $\Gamma_{cb} = 1.6$ cm^{-1}, which is between these two limits. Interestingly, simulations of acetonitrile DOVE spectra place acetonitrile's Γ_{cb} between similar limits.[25] This observation provides evidence that both population and pure dephasing effects are important for CS_2 in solution.

In the observed scans where $\tau_1 = 0.0$ ps and τ_2 is changed, there is an oscillation in intensity of the DOVE feature relative

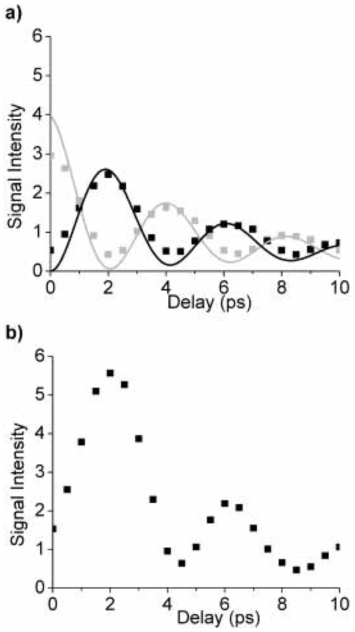

Figure 5. Peak signal intensities of two beating coherences with different dephasing times are simulated in the top graph. Delay represents the time between the pulse generating the coherences and the next pulse. The difference in frequencies (Δ) between the two coherences are 8 cm^{-1}, and the two line widths Γ are 1 and 0.2 cm^{-1}. Solid lines indicate impulse (fs) limit results, whereas squares indicate the result with 1 ps pulses. Lighter values show beating between two pathways of the same sign, whereas the darker values are for opposite signs. DOVE-FWM intensity for the 2 DOVE-IR and 1 DOVE-Raman pathways of equal magnitude are simulated in the bottom graph with 1 ps pulses, $\Delta = 8$ cm^{-1} and (Γ_{cb}, Γ_{ag}) = (1 cm^{-1}, 0.2 cm^{-1}).

to the CARS reference, going from a minimum at $\tau_2 = 0$ ps to a maximum at 2.0 ps and back to a minimum at 4.0 ps. This oscillation is a characteristic of amplitude level interference occurring between the DOVE-IR ρ_{cb} and DOVE-Raman ρ_{ag} coherences at their difference frequency. The frequencies of the two coherences differ by 8 cm^{-1} because of the anharmonicity induced in the a state by the excitation of the b state. Figure 5 shows the results of modeling this behavior for the parameters in Tables 2 and 3 for conditions with the same and opposite signs for the nonlinear polarization in the impulsive limit. The bottom part of Figure 5 shows the results for opposite signs of the nonlinear polarization for 1 ps excitation pulses. This analysis omits contributions from hot band transitions that are also expected to contribute to the beating.

The predicted behavior agrees with that observed in the experiments. Destructive interference occurs at $\tau_2 = 0$ ps because the DOVE-IR and DOVE-Raman processes have opposite signs (see Figure 5). The quantum interference effects damped as a function of the τ_2 delay time if the dephasing rates of the ρ_{cb} and ρ_{ag} coherences differ.

Differences Between Experimental and Simulated Spectra. There are a few features which cannot be readily explained. For example, the FWM data in Figure 3b show a feature at (ω_1, ω_2) = (2210, 1525) cm^{-1} that does not appear in the simulations. This region is complex to simulate because there are contributions from a solvent CARS line at $\omega_1 - \omega_2 = 722$ cm^{-1}, absorption of the excitation beams at $\omega_1 = 2248$ cm^{-1}, a possible SIVE contribution from υ_1, the nearby DOVE resonance, and the background from the sample and windows so further work is required. A second feature appears at (2315, 1517) cm^{-1} which is not represented in the simulated spectrum. It is possible that this second feature may be an additional DOVE peak involving ν_1 and the combination band $\nu_1 + 2\nu_2$ where $2\nu_2$ (bend) = 796 cm^{-1} in neat solution. This peak does appear in the IR spectrum. Such a DOVE peak would involve a Raman transition of $2\nu_2$ which has a Fermi resonance with ν_1. However, it does not appear against the background in any of the other FWM spectra. Scans with $\omega_1 > 2315$ cm^{-1} were not possible because the atmospheric absorption by CO$_2$ was not completely removed in the purging process.

The windows on the sample cell also make a small contribution to the background spectrum because of their nonresonant electronic susceptibility. The back window contribution was neglected because it absorbs the infrared excitation beams and prevents appreciable FWM. The windows are not phase matched because their index of refraction dispersion differs from the sample's so the windows will contribute a complex phase factor to the nonlinear polarization. Although the inclusion of the window contribution explains many of the features seen in the background, it does not adequately describe its slope toward higher ω_1 values. This difference may result from inadequacies in describing the index of refraction dispersion of both the sample and the window. The complex phase angle for the nonlinear polarization is quite sensitive to the exact values of the index of refraction, especially because it changes rapidly near vibrational resonances.[17] There is also a slight discontinuity in the CARS line at the DOVE frequency. This discontinuity may arise from temporal distortions of the excitation beam, since absorption occurs at its central frequency from the infrared absorption, while the wings experience little absorption. These effects were not included in the simulations.

The relative amplitudes of the DOVE-IR and DOVE-Raman pathways are controlled by the dephasing rates, polarizabilities, and transition moments associated with each coherence in the pathway. The polarizabilities and transition moments for the DOVE-IR and DOVE-Raman pathways should be nearly equal ($\alpha_{cb} \sim \alpha_{ag}$, $\mu_{ca} \sim \mu_{bg}$), because both processes involve creation or annihilation of the same vibrational quanta and both polarizabilities are controlled by similar detuning from electronic resonance.[25] If the transition moments and polarizabilities are equal, then $A_{\mathrm{DOVE-IR}} \sim A_{\mathrm{DOVE-Raman}}$. Assuming the values shown in the tables for the dephasing rates, the fitting results show that the values for $A_{\mathrm{DOVE-Raman}}$ are significantly smaller than the values for $A_{\mathrm{DOVE-IR}}$. Any additional DOVE-Raman contribution increases the $\omega_1 - \omega_2$ resonance and causes an increased "tail" on the DOVE peak that is not observed experimentally.

If vibrational transitions are not coupled, it is still possible for a single resonance with one of them to produce a singly vibrationally enhanced (SIVE) feature. SIVE processes are discussed more extensively elsewhere.[26] It is possible that one must consider a SIVE process for strong IR fundamentals such as ν_3 for CS$_2$. However, incorporation of a SIVE term along ω_2 did not improve the agreement with experiment. In addition, it is striking that there is no evidence for a CS$_2$ CARS feature for the υ_3 mode, because no CS$_2$ Raman feature appears when ω_1 is off-resonance. The absence of a CARS peak and the presence of the large DOVE peak show the doubly enhanced process is much stronger than the CARS process for ν_3.

Relationships Between Absorption Coefficients, Raman Cross-Sections, and $\chi^{(3)}$. The DOVE-IR and DOVE-Raman $\chi^{(3)}$ nonlinearities involve the same transition moments as the infrared absorption and Raman cross-sections between the modes involved in the double vibrational resonances. This relationship allows one to make comparisons between the fitted parameters for $\chi^{(3)}$ and the values that are expected from IR and Raman spectra. Vibrational transition dipoles can be readily calculated from line shapes and molar absorptivities in IR

TABLE 3: Summary of Parameters Used for Simulations and Calculations[a]

IR:	$\epsilon(\nu_3)$ (CS_2)	2500 M^{-1} cm^{-1}
	$\epsilon(\nu_1+\nu_3)$ ″	52 M^{-1} cm^{-1}
	$^*n(\nu_1)$	1.43
	$^*n(\nu_1+\nu_3)$	1.44
Raman:	$^*n$(514.5 nm)	1.48
	$(d\sigma_{11}/d\Omega)(CH_2BrCl)$	7.5×10^{-30} cm^2 sr^{-1}
	ω_{eg} (benzene)	52500 cm^{-1}
	* ω_{eg} (CS_2)	48000 cm^{-1}
fitted parameters:	$(A_{DOVE-IR1} \times \hbar)/(A_{CARS(601)} \times \hbar^2)$ (Hz)	-1.2×10^{14}
	$(A_{DOVE-IR2} \times \hbar^2)/(A_{CARS(601)} \times \hbar)$ (Hz)	-1.2×10^{14}
	$(A_{DOVE-Raman} \times \hbar^2)/(A_{CARS(601)} \times \hbar)$ (Hz)	7×10^{13}
	$(A_{CARS(656)} \times \hbar)/(A_{CARS(601)} \times \hbar)$	< 5
	$(A_{Bg} \times \hbar^3)/(A_{CARS(601)} \times \hbar^2)(Hz^{-1})$	3.8×10^{-13}
	$\sigma_1 = \sigma_2 = \sigma_3$ (ps)	0.6
	Γ_{cb} (cm^{-1})	1.6
fixed parameters:	N_{CS2} (M)	0.20
	$N_{CH2BrCl}$(M)	15.1
	l_s (cm)	0.020
	* ω_{eg} (CH_2BrCl)	45000 cm^{-1}

[a] Values with asterisks represent estimations.

spectra, and rotationally averaged polarizabilities can be extracted from Raman cross-section data. The following relationships were used to derive these parameters (ω_L = Raman laser frequency) [13,27−29]

$$(\alpha_{ga}^{XX})^2 = \frac{n(\omega_L)}{n(\omega_L - \omega_{ag})F^2(\omega_L)F^2(\omega_L - \omega_{ag})} \frac{c^4}{\omega_L(\omega_L - \omega_{ag})^3} \times \left(\frac{d\sigma_{11}}{d\Omega}\right)$$

$$\frac{d\sigma_{11}}{d\Omega} = \frac{1}{1+\rho}\left(\frac{d\sigma}{d\Omega}\right)_{||+\perp,90°\text{collection}}$$

$$\mu_{jg} = \sqrt{\frac{n(\omega_{jg})\hbar c \ln(10)\Gamma_{jg}\epsilon_{jg}}{4\pi\omega_{jg}F(\omega_{jg}) \times 1000 N_A}}$$

Here, ϵ_{jg} is the Beer's Law absorptivity on resonance in M^{-1} cm^{-1}, ρ is the depolarization ratio of the given Raman band, and we use CGS units. These equations neglect excited-state populations. Benzene is a reference for Raman cross sections, so a Raman spectrum was acquired with a 10:1:1 CH_2BrCl/CS_2/benzene solution and 514.5 nm excitation with a polarizer in front of the detector in order to determine the Raman cross-section of CH_2BrCl's 601 cm^{-1} mode relative to benzene.[27,30] Because the line-width of dilute CS_2 ($\Gamma_{ag} \sim 0.18$ cm^{-1}) was narrower than the instrumental profile of this Raman system, the literature value for the CS_2 656 cm^{-1} mode's cross section was used instead of deriving it through the deconvolution of the Raman spectrum.[31] The calculated polarizabilities must then be properly corrected for the different excitation frequency and solutions used in the DOVE experiments and the published Raman spectra. The correction depends on the detuning of the excitation from an effective electronic resonance frequency ω_{eg} and the changes in index of refraction and the internal field correction when different solvents are employed. Data for the effective electronic resonance energies of benzene, CS_2, and CH_2BrCl[32−34] shows that ω_{eg} is similar and little dispersion results from this source. These correction factors were used to scale the published Raman cross-sections to the frequency conditions in this experiment.[35] Table 3 contains the summary of the fitting parameters used in the simulations.

One of the significant aspects of DOVE nonlinearities is their sensitivity to the signs of transition moments. The signs cannot be determined from IR, Raman, or CARS spectra which depend quadratically on the transition moments. However, they can be determined in sum frequency generation (SFG)[36] and DOVE experiments where they appear linearly. By examining the interference between CARS and DOVE-Raman processes in CMDVS spectra, one can determine their relative signs. Because the polarizations induced in DOVE-IR and DOVE-Raman must have opposite signs due to a differing number of interactions with the ket vs bra side of the coherences, their interference provides a second measure of the transition moment signs. The results can then be compared with theoretical models.[37,38] DOVE spectroscopy is therefore a useful technique in determining the relative signs of these transitions.

Fitting the simulations with the experimental data provides the nonlinear susceptibilities ($\chi^{(3)}$) and hyperpolarizabilities (γ) of each of the processes relative to CH_2BrCl. The values used for these simulations assume $\omega_2 = 1517$ cm^{-1}, so the DOVE nonlinearities represent doubly resonantly enhanced values. The nonlinearities for each individual pathway are found in the steady state and are related to $P^0(t)$ by

$$\gamma = \frac{2P^0}{NDF(\omega_1)F(\omega_2)F(\omega_3)}; \; \tilde{E}_n(t) = 1$$

$$\chi^{(3)} = N_{neat}F_{neat}(\omega_1)F_{neat}(\omega_2)F_{neat}(\omega_3)\gamma$$

There is a degeneracy factor D from the permutations of the laser frequencies that is introduced by the Maker-Terhune convention.[39] It is 6 for Raman and 3-color FWM experiments. It is 3 for 2-color CARS experiments. $F(\omega_4)$ is absent from these equations. Susceptibilities are more commonly published than hyperpolarizabilities and are usually reported for neat liquids and crystals at each of the FWM frequencies. However, due to the inhomogeneous broadening characteristics of the modes of CS_2 in neat solution and because the index of refraction of bromochloromethane is not well known in the infrared, all values are reported as γ's. The background FWM hyperpolarizability γ_{BG} represents a weighted average of the actual background hyperpolarizabilities of CS_2 and CH_2BrCl; however, because of the large molar ratio of CH_2BrCl over CS_2, the CH_2BrCl

TABLE 4: Hyperpolarizabilities γ_{1111} (cm^6/erg Molecule) Found from the FWM Experiments and Expected Values from the IR-Raman Experiments[a]

	FWM exp	IR-Raman predn
$\gamma_{DOVE-IR1}$	6×10^{-35}	2.0×10^{-34}
$\gamma_{DOVE-IR2}$	7×10^{-35}	2.4×10^{-34}
$\gamma_{\mathrm{DOVE-Raman}}{}^{b}$	-3×10^{-34}	-1.7×10^{-33}
$\mathrm{im}(\gamma_{\mathrm{CARS(656)}})$	$< 2 \times 10^{-35}$	2.6×10^{-35}
$\mathrm{im}(\gamma_{\mathrm{CARS(601)}})$		4.9×10^{-37}
γ_{Bg}	5×10^{-38}	

[a] As comparison, $\gamma_{\mathrm{Raman(992)}}$(benzene) = 1.5×10^{-35} cm^6/erg molecule at 488 nm excitation for a two laser CARS experiment (ref 40). *The $\gamma_{\mathrm{DOVE-Raman}}$ values assume the homogeneous line-width for the ν_1 mode controls the line-width for the DOVE-Raman pathway. If inhomogeneous broadening controls the line-width, the $\gamma_{\mathrm{DOVE-Raman}}$ values will be considerably smaller.

should dominate. The results are shown in Table 4. Comparison between predicted and experimental values of DOVE-IR show reasonable agreement. Interestingly, the FWM experimental value for $\gamma_{\mathrm{DOVE-Raman}}(\mathrm{CS}_2)$ is close to $\gamma_{\mathrm{DOVE-IR}}(\mathrm{CS}_2)$.

Conclusions

The relative intensities of the different features in time-resolved frequency domain two-dimensional DOVE spectra are controlled by a number of factors. The intensity of the DOVE features themselves depends on the interference between the DOVE-Raman and the DOVE-IR coherence pathways and is controlled by the time delay between the infrared pulses and the visible excitation pulse. The features can be suppressed or enhanced by adjusting the time delays to attain the proper phase. The intensity of the background depends on the very rapidly dephasing electronic coherences and is controlled by the temporal overlap of the three excitation beams. The intensities of CARS features depend on both the rapid dephasing rates of the electronic coherence and slower dephasing rates of the vibrational coherences. The electronic coherences are controlled by the temporal overlap of the two infrared pulses and vibrational coherences are controlled by the time delay between the infrared pulses and the visible excitation pulse. This paper demonstrated that background and CARS suppression and DOVE enhancement and suppression is achievable for 2D DOVE-FWM spectra using picosecond pulses. More complete suppression and control is expected when shorter pulses are used. These capabilities provide the opportunity for optimizing the relative intensities of different spectral features when these 2D methods are applied to chemical measurements.

Acknowledgment. This research has been supported by the Chemistry Division of the National Science Foundation under grant CHE-0130947.

References and Notes

(1) Wright, J. C. *Int. Rev. Phys. Chem.* **2002**, *21*, 185.

(2) Scheurer, C.; Mukamel, S. *Bull. Chem. Soc. Jpn.* **2002**, *75*, 989.

(3) Zanni, M. T.; Asplund, M. C.; Hochstrasser, R. M. *J. Chem. Phys.* **2001**, *114*, 4579.

(4) Zhao, W.; Wright, J. C. *Phys. Rev. Lett.* **2000**, *84*, 1411.

(5) Zhao, W.; Wright, J. C. *Phys. Rev. Lett.* **1999**, *83*, 1950.

(6) Daniel, C.; Full, J.; Gonzalez, L.; Lupulescu, C.; Manz, J.; Merli, A.; Vajda, S.; Woste, L. *Science* **2003**, *299*, 536.

(7) Rice, S. A. *Science* **1992**, *258*, 412.

(8) Rabitz, H.; de Vivie-Riedle, R.; Motzkus, M.; Kompa, K. *Science* **2000**, *288*, 824.

(9) Tannor, D. J.; Rice, S. A. *J. Chem. Phys.* **1985**, *83*, 5013.

(10) Tannor, D. J.; Rice, S. A. *Adv. Chem. Phys.* **1988**, *70*, 441.

(11) Levis, R. J.; Menkir, G. M.; Rabitz, H. *Science* **2001**, *292*, 709.

(12) Meyer, K. A.; Wright, J. C. *Anal. Chem.* **2001**, *73*, 5020.

(13) Mukamel, S. *Principles of Nonlinear Optical Spectrscopy*, 1st ed.; Oxford University Press: New York, 1995.

(14) Armstrong, J. A.; Bloembergen, N.; Ducuing, J.; Pershan, P. S. *Phys. Rev.* **1962**, *127*, 1918.

(15) Murry, R. L.; Fourkas, J. T.; Keyes, T. *J. Chem. Phys.* **1998**, *109*, 2814.

(16) Nestor, J. R.; Lippencott, E. R. *J. Raman Spectrosc.* **1973**, *1*, 305.

(17) Thompson, D. E.; Wright, J. C. *J. Phys. Chem. A* **2000**, *104*, 11282.

(18) Murdoch, K. M.; Thompson, D. E.; Meyer, K. A.; Wright, J. C. *Appl. Spectrosc.* **2000**, *54*, 1495.

(19) Carlson, R. J.; Wright, J. C. *Appl. Spectrosc.* **1989**, *43*, 1195.

(20) Tolles, W. M.; Nibler, J. W.; McDonald, J. R.; Harvey, A. B. *Appl. Spectrosc.* **1977**, *31*, 253.

(21) Kamga, F. M.; Sceats, M. G. *Opt. Lett.* **1980**, *5*, 126.

(22) Kim, Y. I.; Shin, K. J. *Bull. Korean Chem. Soc.* **1987**, *88*, 105.

(23) Aechtner, P.; Lauberau, A. *Chem. Phys.* 1991, *149*, 419.

(24) Besemann, D. M.; Condon, N. J.; Murdoch, K. M.; Meyer, K. A.; Zhao, W.; Wright, J. C. *Chem. Phys.* **2001**, *266*, 177.

(25) Wright, J. C.; Condon, N. J.; Murdoch, K. M.; Besemann, D. M.; Meyer, K. A. *J. Phys. Chem.* 2003, in press.

(26) LaBuda, M. J.; Wright, J. C. *J. Chem. Phys.* 1998, *108*, 4112.

(27) Schomacker, K. T.; Delaney, J. K.; Champion, P. M. *J. Chem. Phys.* **1986**, *85*, 4240.

(28) Montero, S. *J. Chem. Phys.* **1982**, *77*, 23.

(29) Condon, N. J. Doubly Vibrationally Enhanced Infrared Four Wave Mixing Spectroscopy of Acetonitrile and Crotonitrile, University of Wisconsin, 2001.

(30) Levenson, M. D.; Bloembergen, N. *Phys. Rev. B* **1974**, *10*, 4447.

(31) Kato, Y.; Takuma, H. *J. Opt. Soc. Am.* 1971, *61*, 347.

(32) Asher, S. A.; Johnson, C. R. *J. Phys. Chem.* **1985**, *89*, 1375.

(33) Ci, X.; Myers, A. B. *J. Chem. Phys.* **1992**, *96*, 6433.

(34) Man, S. Q.; Kwok, W. M.; Phillips, D. L. *J. Chem. Phys.* **1996**, *105*, 5842.

(35) Tang, A.; Albrecht, A. C. Developments in the Theories of Vibrational Raman Intensities. In *Raman Spectroscopy- Theory and Practice*; Szymanski, H. A., Ed.; Plenum Press: New York, 1970; Vol. 2; p 36.

(36) Hayashi, M.; Lin, S. H.; Raschke, M. B.; Shen, Y. R. *J. Phys Chem A* **2002**, *106*, 2271.

(37) Fernandez-Sanchez, J. M.; Montero, S. *J. Chem. Phys.* **1989**, *90*, 2909.

(38) Kwak, K.; Cha, S.; Cho, M.; Wright, J. C. *J. Chem. Phys.* **2002**, *117*, 5675.

(39) Maker, P. D.; Terhune, R. W. *Phys. Rev.* **1965**, *137*, A801.

(40) Levenson, M. D.; Bloembergen, N. *J. Chem. Phys.* **1974**, *60*, 1323.